Journal of ELECTRONIC MATERIALS, Vol. 45, No. 7, 2016
DOI: 10.1007/s11664-016-4518-1

Effect of Heat Treatment Under Nitrogen Atmosphere on Sprayed Fluorine Doped In_2O_3 Thin Films

NASREDDINE BEJI,[1,2] MEJDA AJILI,[1] and NAJOUA KAMOUN TURKI[1]

1.—Université de Tunis El Manar, Faculté des Sciences de Tunis, Département de Physique, LR99ES13 Laboratoire de Physique de la Matière Condensée (LPMC), 2092 Tunis, Tunisia.
2.—e-mail: beji.nasreddine@yahoo.fr

Fluorine-doped indium oxide thin films (In_2O_3:F) were prepared at 500°C for different fluorine concentrations (0 at.%, 2 at.%, 6 at.% and 10 at.%) using the chemical spray pyrolysis technique. Structure and surface morphology of these films were characterized by x-ray diffraction (XRD) and atomic force microscopy (AFM). XRD analysis revealed that fluorine doped In_2O_3 thin films exhibit a centered cubic structure with the (400) preferential orientation. The change of the preferential reflection plane from (222) to (400) was found after doping. The doping optimum concentration of thin film crystal structure is obtained witha fluorine ratio equal to 2 at.%. The crystallinity improvement of In_2O_3:F (2 at.%) film is detected after annealing at 200°C, 300°C, and 400°C in nitrogen gas for 45 min. Transmission and reflection spectra measurements were performed over the wavelength range of 250–2500 nm. The band gap energy increase from 3.10 eV to 3.45 eV was detected after treatment at 400°C. In parallel, the electrical resistivity, deduced from Hall effect measurements, decreases from 428.90 $\times$ 10^{-4} Ω cm to 6.58 $\times$ 10^{-4} Ω cm.

Key words: Thin films, chemical spray pyrolysis, fluorine doped indium oxide, annealing under nitrogen gas

INTRODUCTION

Transparent conducting oxide (TCO) films, such as In_2O_3, are interesting for many research and industrial applications including photovoltaic devices,[1] transparent conductive electrodes,[2] and gas sensors.[3] This is mainly due to its important properties like chemical stability, nontoxicity, high transmittance,[4] wide band gap[5,6] and low resistivity.[7–9] Furthermore, indium oxide films exhibit an *n*-type conductivity. In_2O_3 thin films can be prepared with high reproducibility using various methods including reactive direct current (DC) magnetron sputtering deposition,[10] vacuum thermal evaporation,[11] pulsed laser ablation,[12] sol–gel technique,[13] and spray pyrolysis.[4,14,15] Among these methods, spray pyrolysis, which is a chemical deposition technique, offers many advantages such as low cost, simplicity, and easy adaptability for large-area film fabrication.

Fluorine doped In_2O_3 thin films were the focus of several studies.[9,15,16] In our knowledge, there was no study of physical properties of In_2O_3:F elaborated by spray pyrolysis and treated at different temperatures in nitrogen atmosphere.

In this work, different fluorine doping concentrations $y = [F^-]/[In^{3+}]$ = 0 at.%, 2 at.%, 6 at.%, and 10 at.% were taken. Then, we have investigated their influence on the crystalline structure of indium oxide thin films. Furthermore, the heat treatment of the 2 at.% doped samples was performed at temperatures of 200°C, 300°C, and 400°C for 45 min in order to optimize the structural, morphological, electrical, and optical properties. Such analytic techniques as x-ray diffraction (XRD), atomic force microscopy (AFM), and spectrophotometry have been used to determine crystalline structure, surface morphology, and electrical and optical properties. The improvement of physical properties of In_2O_3:F allows using the material as

(Received September 1, 2014; accepted April 6, 2016; published online April 19, 2016)

optical windows or transparent conductive electrodes in photovoltaic devices.

EXPERIMENTAL DETAILS

Fluorine-doped indium oxide thin layers were prepared by the chemical reactive liquid phase (spray) pulverization on glass substrates heated up to 500°C. The aqueous solution contains indium chloride ($InCl_3$) and ammonium fluoride (NH_4F) which is used as the doping agent. Compressed air was used as a carrier gas. The solution flow rate is set to 2.5 ml min^{-1}. The distance between nozzle and sample is 28 cm. The experimental setup, installed in our laboratory and used to spray indium oxide thin layers, includes a heating system for glass substrates and a nozzle fixed on the two-dimensional moving table allowing pulverization of the whole isothermal zone containing heated substrates.[17] The atomic concentration of fluorine in the solution was taken as y = 0 at.%, 2 at.%, 6 at.%, and 10 at.%. The film structure was studied by XRD using an automated Bruker D8 Advance diffractometer for the 2θ range of 10°–80°. The wavelength, accelerating voltage, and current were 1.5418 Å, 40 kV and 20 mA, respectively. The crystallinity of the films was also examined by a Raman spectrometer. The micro-Raman scattering spectra were recorded by a Jobin–Yvon technology Labram Horiba Raman (HR) scientificinstrument equipped with a He–Ne laser (632.8 nm). The investigated spectral range was between 100 cm^{-1} and 600 cm^{-1}. The film surface morphology was studied by Atomic Force Microscopy (AFM, a standard Veeco Dimension 3100, used in tapping mode). The optical transmission and reflection measurements were carried out with a Perkin-Elmer Lambda 950 spectrophotometer in the wavelength range of 250–2500 nm at room temperature taking air as a reference. Resistivity, carrier concentration, and mobility were determined from Hall effect measurements in the Van Der Pauw configuration.

RESULTS AND DISCUSSION

Variation of Fluorine Doped Concentration

Structural Properties

Figure 1 presents XRD spectra of fluorine doped indium oxide thin films, grown for different concentrations of 0 at.%, 2 at.%, 6 at.%, and 10 at.% at a substrate temperature equal to 500°C. All the diffraction patterns correspond to the centered cubic structure of In_2O_3 material as revealed from XRD (JCPDF n° 06-0416). Sharp peaks were observed at 2θ = 30.52° and 35.32°, and these were assigned to the (222) and (400) planes, respectively. Reflection peaks were very narrow indicating good crystallinity. Parthiban et al.[18] shows a similar change in the preferred orientation from (222) to (400) after doping In_2O_3 thin films with molybdenum.

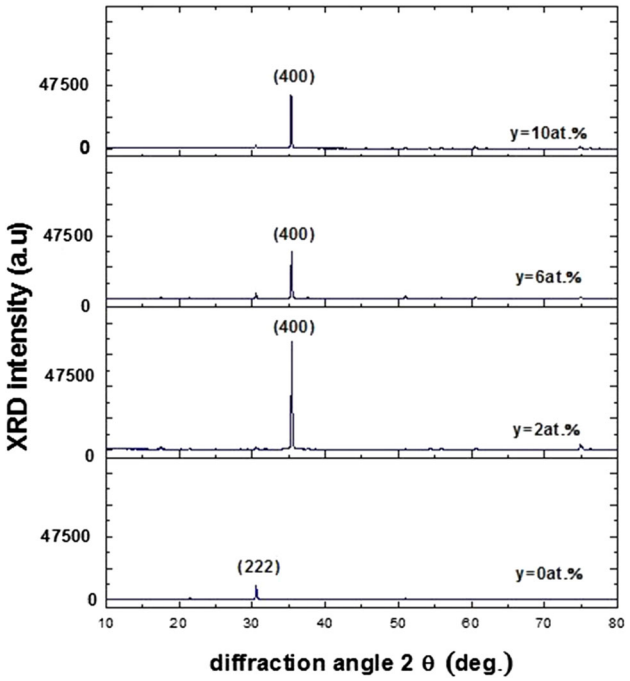

Fig. 1. XRD pattern of fluorine doped indium oxide thin films grown at different fluorine doping concentrations $y = [F^-]/[In^{3+}]$.

The lattice parameter of In_2O_3:F (2 at.%) thin films was calculated using MAUD (Material Analysis Using Diffraction) software based on XRD spectra. The value of 10.102 Å is lower than that of the In_2O_3 bulk (a = 10.118 Å). This can be due to the F^- substitution for the O^{2-} ions. Indeed, the F^- radius is lower than that of O^{2-} and it is higher than that of In^{3+}.

After doping, the increase of preferential diffraction peak intensity corresponds to an enhancement of the crystallinity. This crystallinity improvement could be due to the fluorine occupation of the oxygen vacancies or due to the substitution of O^{2-} by F^-. The strong and sharp (400) peak was observed at y = 2 at.% indicating the best film crystallinity. Beyond 2 at.% doping, a deterioration of thin films crystallinity was noticed on the fluorine ratio increase, which may be due to the F^- incorporation into the interstitial sites. Moreover, this effect may be a result of formation of stress caused by the difference in ion size between oxygen and fluorine in the lattice. A similar phenomenon was observed by Zi-qiang et al.[19] for ZnO:Al thin films.

The average grain size (d) was estimated by the Scherrer's formula[20]:

$$d = \frac{0.94\lambda}{\sqrt{\beta - \beta_0}x\cos\theta}, \qquad (1)$$

where λ is the x-ray wavelength of Cu Kα radiation (λ = 1.5418 Å), β_0 is the width of the corresponding peak due to the instrumental expansion, which is about 0.125°. β is the experimental full-width at

half-maximum (FWHM) of the (400) diffracted peak measured in radians and θ is the Bragg's angle.

The d values obtained for different fluorine concentrations are presented in Table I.

Beyond 2 at.%, the average grain size decreased but is still greater than undoped thin films. This behavior could be related to the difference between ionic radii of F^- (133 pm) and O^{2-} (140 pm) ions.[17] The maximum of d which is equal to 78.4 nm was obtained for y = 2 at.%, corresponding to the best crystallinity.

The Raman spectrum, shown in Fig. 2, was used to determine vibration modes of In_2O_3:F (2 at.%). In the range of 100–600 cm^{-1}, the spectrum shows the expected vibrational modes at 109 cm^{-1}, 133 cm^{-1}, 306 cm^{-1}, 366 cm^{-1}, 495 cm^{-1} and 517 cm^{-1}, which are certainly characteristic of the In_2O_3 Raman spectra, as reported by Berengue et al.[21] The body centered cubic In_2O_3 belongs to the space group $Ia3$, $Th7$.

For this structure, predicted modes[22,23] are: $4A_g$ (Raman), $4E_g$ (Raman), $14T_g$ (Raman), $5A_u$ (inactive), $5E_u$ (inactive), and $16T_u$ (infra-red).

The vibrations with symmetry A_g, E_g, and T_g are Raman active and infrared inactive, and the T_u vibrations are infrared active and Raman inactive. The A_u and E_u vibrations are inactive in both infrared and Raman measurements.

Morphological Properties

Figure 3 shows the atomic force microscopy (AFM) images of undoped and In_2O_3:F (2 at.%) thin films. All films have almost uniform morphology and compact structure. These images show that surface morphologies were strongly dependent on dopant concentration. In fact, atomic force microscopy (AFM) images revealed that crystallite shapes were affected by the preferred orientation change. A similar result was obtained by Castañeda et al.[24] Surface morphology observations indicate that crystallite size increases after doping that agrees with the XRD results. The grain size seen from AFM images is increasing after doping, which is in accordance with calculated grain size using Sherrer's formula (Table I).

Conclusion

From the structural and morphological analysis, it is clear that the optimal fluorine doping level is 2 at.%. For this reason, the In_2O_3:F (2 at.%.) layers were selected for annealing at temperatures T_a = 200°C, 300°C, and 400°C in N_2 gas to improve their physical properties.

Heat Treatment Effect

Structural Properties

Figure 4 shows XRD patterns of annealed In_2O_3:F (2 at.%) films. All the annealed In_2O_3:F (2 at.%) thin films are polycrystalline with a cubic centered In_2O_3 structure. Thus, the cubic structure of In_2O_3:F (2 at.%) is stable on annealing. Observed peaks remain very narrow showing a good crystallinity after heat treatment. Moreover, thin films exhibit stronger (400) preferred orientation, which indicates that crystalline quality is enhanced as the annealing temperature is increased. Beyond 200°C, the diffraction intensity peaks does not change noticeably, which indicates that crystallization was completed at T_a = 200°C. A similar result has been reported by Sun et al.[25]

After annealing, the grain size (d) was calculated using Scherrer's formula, and the dislocation density (δ_{disc}) and crystallites number per unit surface area (n_c) by relations[20]:

$$\delta_{disc} = \frac{1}{d^2} \tag{2}$$

$$n_c = \frac{t}{d^3}, \tag{3}$$

where t is the film thickness.

The parameters d, δ_{dis} and n_c are presented in Fig. 5 as functions of T_a.

The grain size increases reaching the maximum of ~83.8 nm at T_a = 200°C. This grain size increase

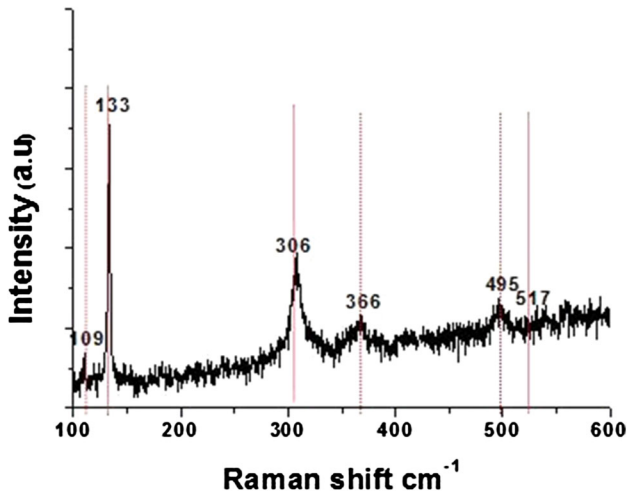

Fig. 2. Raman scattering measurements of sprayed In_2O_3:F (2 at.%).

Table I. Grain size of In_2O_3 thin films grown for different atomic concentrations y

y (at.%)	0	2	6	10
d (nm)	55.8	78.4	74.6	75.5

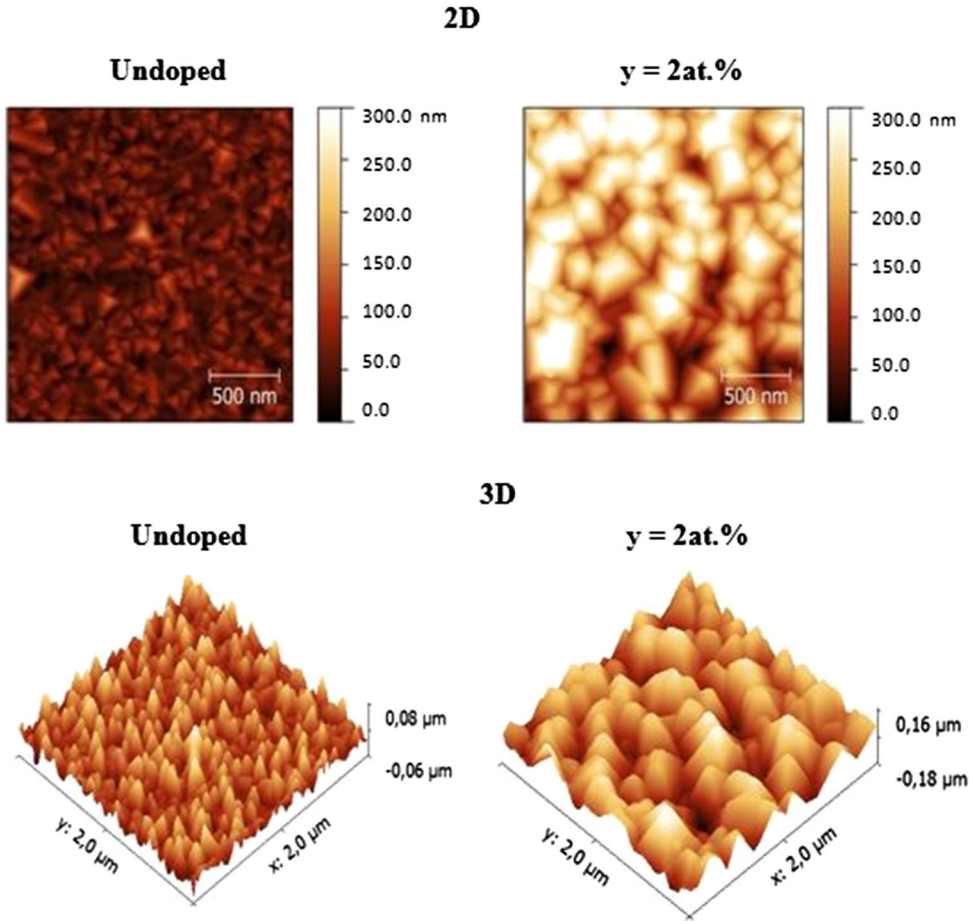

Fig. 3. Atomic force microscopy (AFM) images of In_2O_3:F thin films grown at different fluorine doping concentrations y (undoped and 2 at.%).

indicates the film crystallinity improvement. Similar results were obtained by Yuan et al.[26] for the In_2O_3 films annealed in vacuum and air.

Moreover, the dislocation density and crystallites number decrease from 1.6 to 1.4×10^{10} cm^{-2} and from 7.8 to 6.3×10^{12} cm^{-2}, respectively, after annealing at 200°C.

Above 200°C, the curves show that each structural parameter has approximately the same value, reaching a saturation region.

Morphological Properties

Atomic force microscopy (AFM) images of In_2O_3:F (2 at.%) thin films before and after annealing at 400°C are presented in Fig. 6. A slight crystallite size increase is observed after annealing that verifies the XRD results.

Electrical Properties

The electrical parameters of annealing In_2O_3:F (2 at.%) thin films are listed in Table II. The sign of the Hall Effect coefficient confirms the n-type of the indium oxide semi conductor after doping. Figure 7 shows the variation of electrical resistivity of In_2O_3:F (2 at.%) films before and after annealing under nitrogen atmosphere at different temperatures. The resistivity decreased from 428.90×10^{-4} Ω cm to 54×10^{-4} Ω cm after annealing at 200°C. The minimum value of 6.58×10^{-4} Ω cm was reached at T_a = 400°C. This resistivity value is better than those in other fluorine doped indium oxide thin films elaborated by different methods.[1,15] The resistivity decrease can be attributed to the carrier concentration increase of by two orders of magnitude, as revealed in Table II. A similar result was obtained by Yuan et al. for the In_2O_3 thin films annealed in vacuum.[26] In fact, Yuan et al.[26] shown that annealing In_2O_3 thin films at 500°C under vacuum for an hour leads to a decrease of electrical resistivity (1.05×10^{-3} Ω cm) and an increase of the carrier concentration (2.80×10^{20} cm^{-3}). Our experimental results confirm good annealing efficiency in nitrogen instead of in a vacuum. Indeed, we have annealed at a lower temperature (400°C) with lower duration (45 min), and we obtained better experimental values of resistivity. This crucial decrease in resistivity can be attributed to an increase of the charge mobility after annealing (Table II)[26] or due to an increase in the grain size

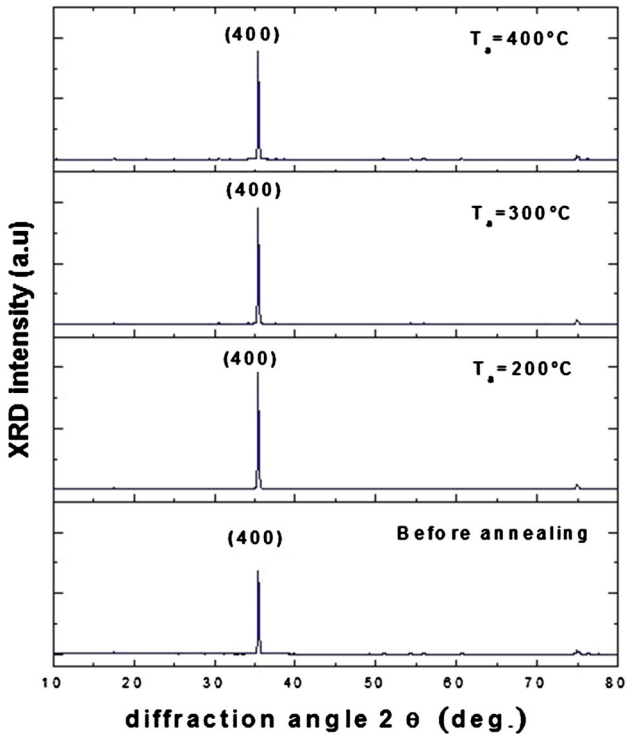

Fig. 4. XRD patterns of 2 at.% fluorine doped indium oxide thin films as a function of annealing temperature (T_a).

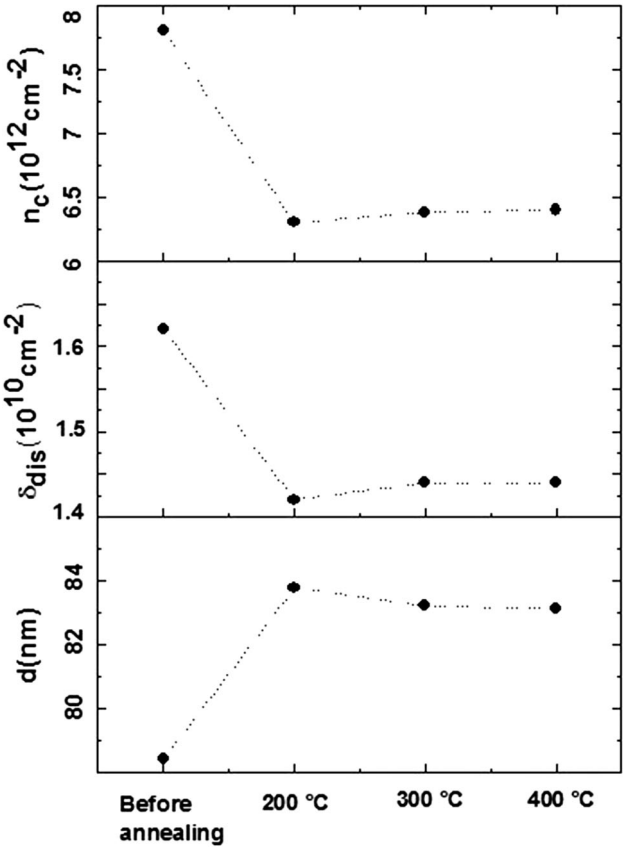

Fig. 5. Variations of grain size (d), number of crystallites (n_c) and dislocation density (δ_{dis}) per unit surface area as a function of annealing temperatures.

of the films[27] as illustrated previously in our structural analysis. Moreover, free volume carrier concentrations N_v and N_s (Table II) increased sharply as a function of annealing temperature, which can be a good factor to improve the degenerate character of the films. Indeed, the fluorine doped indium oxide films have high free volume carrier concentration values ($>10^{20}$ cm^{-3}).

Optical properties

Figure 8 shows optical transmittance and reflection spectra of annealed In_2O_3:F (2 at.%) thin films. The In_2O_3:F (2 at.%) film transparency is improved after annealing. However, a decrease of the transmittance in IR region as a function of annealing temperature was observed, which may be due to the increase of free carrier concentrations (N_s and N_v) after annealing as revealed from Table II.

The band gap value can be obtained from the optical absorption spectra using Tauc's relation[28]:

$$(\alpha h\nu) = A(h\nu - E_g)^n, \tag{4}$$

where $(h\nu)$ is the photon energy, h is Planck's constant, E_g is the optical band gap, n is equal to ½ for direct band gap, A is a constant, and α is the absorption coefficient, which can be calculated using this formula:

$$\alpha = -\frac{1}{t} Ln\left[\frac{T}{(1-R)^2}\right], \tag{5}$$

where t, T, and R are respectively the film thickness, transmittance, and reflectance.

The thickness t of the indium oxide thin layers can be calculated using the weight difference method with the following relation used by Yahmadi et al. for In_2S_3 material[29]:

$$t = \frac{m}{d \cdot S}, \tag{6}$$

where m is the mass of the thin layer deposited on the glass substrate expressed in grams, d is the density of the indium oxide thin films in the bulk form and S (cm^2) is the effective area of the glass substrate on which the film was deposited.

Figure 9 shows the variation of $(\alpha h\nu)^2$ versus $(h\nu)$ for the In_2O_3:F. The straight line of films over the wide range of photon energy indicates the direct type transition. The direct band gap energy was obtained by extrapolating the linear part of the Tauc plot curves to intercept the energy axis (at $\alpha h\nu = 0$). Estimated values of E_g for indium oxide films decreases after doping with fluorine from 3.42 eV to 3.10 eV. This difference in the band gap energy with doping may be due to the changes in morphological, structural, and electrical behaviors

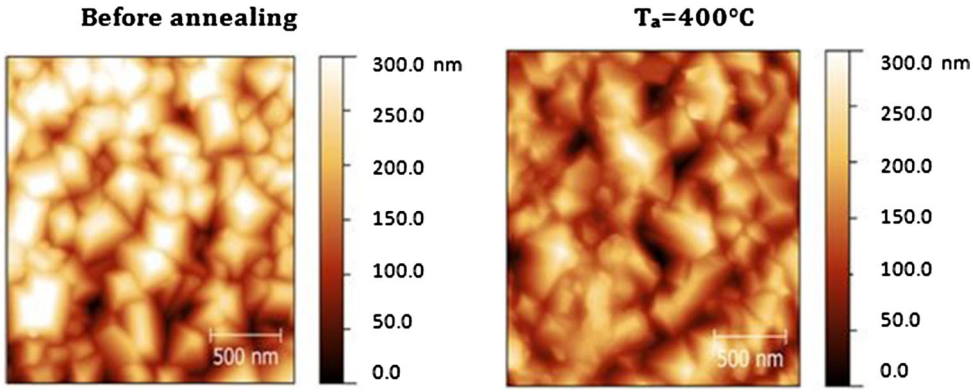

Fig. 6. Atomic force microscopy (AFM) images of In_2O_3:F (2 at.%) thin films before annealing and annealed at 400°C.

Table II. Resistivity (ρ), Hall mobility (μ), and carrier concentrations (volume N_v and surface N_s) of In_2O_3:F thin films as a function of annealing temperatures

Samples	T_a (°C)	ρ (Ω cm) × 10^{-4}	μ (cm^{-2} V^{-1} s^{-1})	N_v (cm^{-3}) × 10^{20}	N_s (cm^{-2}) × 10^{14}
In_2O_3:F (2 at.%)	Before annealing	428.90	4.56	0.32	9.57
	200	54.00	12.20	0.94	28.30
	300	8.93	10.70	6.55	197
	400	6.58	11.34	24.30	728

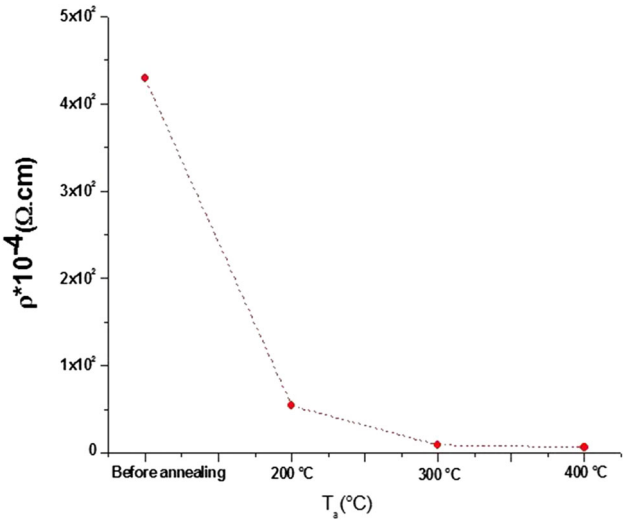

Fig. 7. Resistivity of In_2O_3:F (2 at.%) thin films before and after annealing in nitrogen at different annealing temperatures T_a.

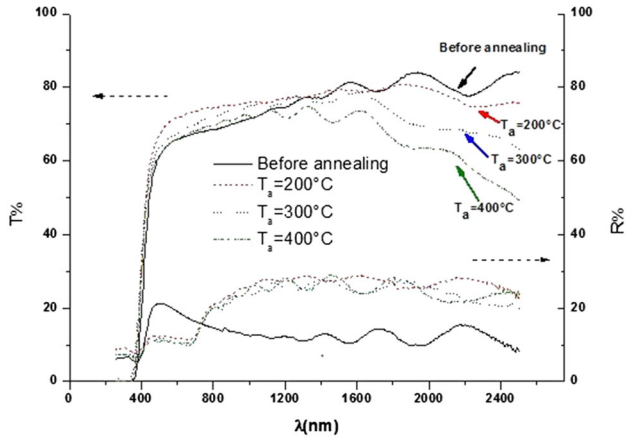

Fig. 8. Transmission and reflection spectra of [In_2O_3:F (2 at.%)] thin films deposited on glass substrates before and after heat treatment under nitrogen at different annealing temperatures (T_a).

of the films. Similar results were found by Kamoun Allouche et al. for $CuInS_2$ material.[30]

Optical band gap of the In_2O_3:F (2 at.%) (Fig. 9), which is in the order of 3.10 eV before heating, increases to 3.45 eV after annealing at 400°C.

Figure of Merit

For transparent conductive oxide films, optical and electrical properties are very important. Perfectly, optical transmittance and electrical conduction should be as large as possible.

Using Haacke's equation[31] we have calculated the figure of merit (ϕ):

$$\phi = \frac{T^{10}}{R_s}, \tag{7}$$

where T is the transmittance at 550 nm wavelength and R_s is the sheet resistance ($R_s = \rho/t$).

Figure 10 exhibits the figure of merit ϕ as a function of annealing temperature. ϕ increases from

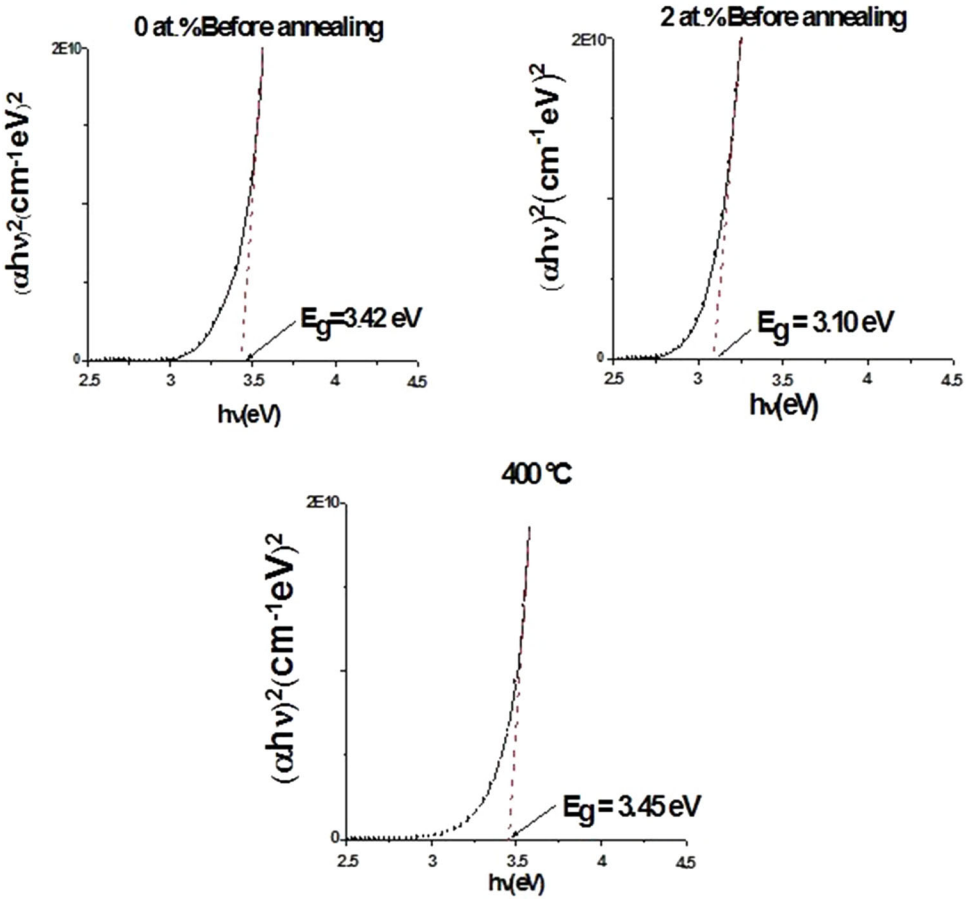

Fig. 9. Variation $(\alpha h\nu)^2 = f(h\nu)$ of undoped indium oxide thin films and In_2O_3:F (2 at.%) before annealing and for In_2O_3 (2 at.%) annealed at 400°C.

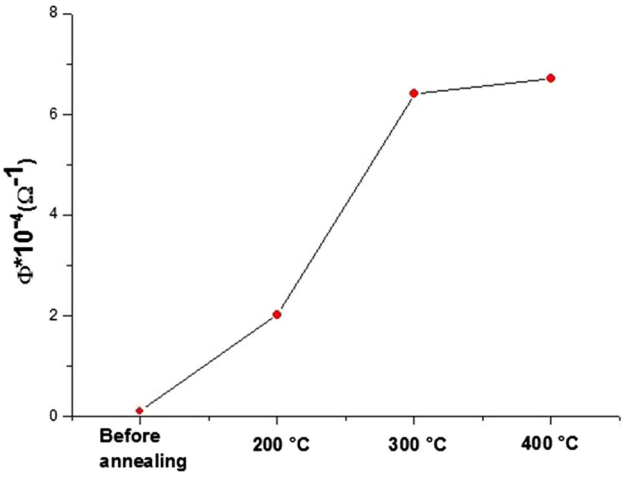

Fig. 10. Figure of merit Φ as a function of annealing temperature for In_2O_3:F (2 at.%).

$0.1 \times 10^{-4}\,\Omega^{-1}$ to $6.4 \times 10^{-4}\,\Omega^{-1}$ in as deposited and annealed (400°C) In_2O_3:F (2 at.%) thin films.

The crucial decrease of the sheet resistance is the main factor for the increase of the figure of merit. The best TCO corresponds to the films annealed at 400°C.

CONCLUSION

Fluorine-doped indium oxide films were deposited by spray pyrolysis technique for different fluorine content equal to 0 at.%, 2 at.%, 6 at.%, and 10 at.%. The XRD experimental results reveal that the predominant orientation after doping with fluorine is (400) indicating a cubic centered structure. The best crystallinity was found at a doping level of 2 at.%. After annealing at 200°C, 300°C, and 400°C, structural properties of thin films were improved as revealed from the increase of XRD intensity peaks. Electrical properties show a decrease of resistivity for annealed thin films and reach a minimum value of $6.58 \times 10^{-4}\Omega$ cm at an annealing temperature of 400°C. The band gap increases also with annealing temperatures to reach a value of 3.45 eV at 400°C.

Thus, the annealing at 400°C is most suitable for production of good In_2O_3:F thin films. In addition, it is important to note that a treatment under nitrogen atmosphere is sufficient to improve the physical properties of fluorine doped indium oxide thin films. This will allow us to use this material as optical

windows or transparent conductive electrodes in photovoltaic devices.

ACKNOWLEDGEMENTS

The authors wish to thank Mr. Mehdi Souli from Laboratoire de Physique de la Matière condensée LR99ES13, Faculté des Sciences de Tunis, Tunis El Manar 2092, Tunisia.

REFERENCES

1. A. El Hichou, M. Addou, M. Mansori, and J. Ebothé, *Sol. Energy Mater. Sol. Cells* 93, 609 (2009).
2. A. Ali, A. Shuhaimi, and Z. Hassan, *Appl. Surf. Sci.* 288, 599 (2014).
3. G. Korotcenkov, I. Boris, V. Brinzari, V. Golovanov, Yu Lychkovsky, G. Karkotsky, A. Cornet, E. Rossinyol, J. Rodrigue, and A. Cirera, *Sens. Actuators B* 103, 13 (2004).
4. J. Joseph Prince, S. Ramamurthy, B. Subramanian, C. Sanjeeviraja, and M. Jayachandran, *J. Cryst. Growth.* 240, 142 (2002).
5. L.J. Meng and M.P. Dos Santos, *Thin Solid Films.* 322, 56 (1998).
6. M. Bender, W. Seelig, C. Daube, H. Frankenberger, B. Ocker, and J. Stollenwrek, *Thin Solid Films* 326, 72 (1998).
7. E. Benamar, M. Rami, C. Messaoudi, D. Sayah, and A. Ennaoui, *Sol. Energy Mater. Sol. Cells* 56, 125 (1999).
8. A. Moses Ezhil Raj, K.C. Lalithambika, V.S. Vidhya, G. Rajagopal, A. Thayumanavan, M. Jayachandran, and C. Sanjeeviraja, *Phys. B* 403, 544 (2008).
9. S.M. Rozati and Z. Bargbidi, *World Renew. Energy Congr.* (2011). doi:10.3384/ecp110572795.
10. Y.S. Jung, D.W. Lee, and D.Y. Jeon, *Appl. Surf. Sci.* 221, 136 (2004).
11. C. Cantalini, W. Wlodarski, H.T. Sun, M.Z. Atashbar, M. Passacantando, A.R. Phani, and S. Santucci, *Thin Solid Films* 350, 276 (1999).
12. D. Beena, K.J. Lethy, R. Vinodkumar, V.P. Mahadevan Pillai, V. Ganesan, D.M. Phase, and S.K. Sudheer, *Appl. Surf. Sci.* 255, 8334 (2009).
13. J. Liu, D. Wu, and S. Zeng, *J. Mater. Process. Technol.* 209, 3943 (2009).
14. P. Prathap, Y.P.V. Subbaiah, M. Devika, and K.T. Ramakrishna Reddy, *Mater. Chem. Phys.* 100, 375 (2006).
15. N. Fellahi, M. Addou, Z. Sofiani, M. El Jouad, K. Bahedi, S. Bayoud, M. Haouti, B. Sahraoui, and J.C. Bernede, *J. Optoelectron. Adv. Mater.* 12, 1087 (2010).
16. D.W. Sheel and J.M. Gaskell, *Thin Solid Films* 520, 1242 (2011).
17. M. Ajili, M. Castagné, and N. KamounTurki, *Superlattices Microstruct.* 53, 213 (2013).
18. S. Parthiban, E. Elangovan, K. Ramamurthi, R. Martins, and E. Fortunato, *Sol. Energy Mater. Sol. Cells* 94, 406 (2010).
19. X. Zi-qiang, D. Hong, L. Yan, and C. Hang, *Mater. Sci. Semicond. Process.* 9, 132 (2006).
20. A. Akkari, M. Reghima, C. Guasch, and N. Kamoun, Turki. *J. Mater. Sci.* 47, 1365 (2012).
21. O.M. Berengue, A.D. Rodrigues, C.J. Dalmaschio, A.J.C. Lanfredi, E.R. Leite, and A.J. Chiquito, *J. Phys. D* 43, 045401 (2010).
22. Ch.Y. Wang, Y. Dai, J. Pezoldt, B. Lu, Th. Kups, V. Cimalla, and O. Ambacher, *Cryst. Growth Des.* 8, 4 (2008).
23. R.K. Gupta, K. Ghosh, S.R. Mishra, and P.K. Kahol, *Appl. Surf. Sci.* 254, 4018 (2008).
24. L. Castañeda, A. Maldonado, J. Vega Pérez, M. de la L. Olvera, and C. Torres-Torres, *Mater. Sci. Semicond. Process.* 26, 288 (2014).
25. K. Sun, W. Zhou, X. Tang, Z. Huang, F. Luo, and D. Zhu, *Surf. Coat. Technol.* 206, 4095 (2012).
26. Z. Yuan, X. Zhu, X. Wang, X. Cai, B. Zhang, D. Qiu, and H. Wu, *Thin Solid Films* 519, 3254 (2011).
27. S. Erat, H. Metin, and M. Ari, *Mater. Chem. Phys.* 111, 114 (2008).
28. J. Tauc and A. Menth, *J. Non-Cryst. Solids* 8–10, 569 (1972).
29. B. Yahmadi, N. Kamoun, C. Guasch, and R. Bennaceur, *Mater. Chem. Phys.* 127, 239 (2011).
30. N. Kamoun Allouche, N. Jebbari, C. Guasch, and N. Kamoun Turki, *J. Alloys Compd.* 501, 85 (2010).
31. A.V. Moholkar, S.M. Pawar, K.Y. Rajpure, V. Ganesan, and C.H. Bhosale, *J. Alloys Compd.* 464, 387 (2008).